RMetS
Royal Meteorological Society

Gravity-wave-induced perturbations in marine stratocumulus

G. Allen,[a*] G. Vaughan,[a] T. Toniazzo,[b] H. Coe,[a] P. Connolly,[a] S. E. Yuter,[c] C. D. Burleyson,[c] P. Minnis[d] and J. K. Ayers[e]

[a]*Centre for Atmospheric Science, University of Manchester, UK*
[b]*Department of Meteorology, University of Reading, UK*
[c]*Department of Marine, Earth and Atmospheric Sciences North Carolina State University, Raleigh, NC, USA*
[d]*NASA Langley Research Center, USA*
[e]*Science Systems and Applications, Incorporated, USA*

*Correspondence to: G. Allen, University of Manchester, Centre for Atmospheric Science, Simon Building, University of Manchester, Oxford Rd, Manchester M13 9PL, UK. E-mail: grant.allen@manchester.ac.uk; grant.allen1@gmail.com

We discuss the role of atmospheric gravity waves in modulating cloud radiative and dynamical properties over the southeast Pacific. Satellite imagery and satellite-retrieved cloud properties during October 2008 illustrate three distinct episodes of horizontal propagation of gravity wave trains across the large-scale stratocumulus (Sc) cloud deck capping the local marine boundary layer. In one period, 7–9 October 2008, the waves modulated cloud-top-height by up to 400 m peak-to-trough, propagating perpendicular to the synoptic boundary layer flow with phase speed 15.3 m s^{-1}, period $\sim$1 h and horizontal wavelength 55 km. The gravity waves were observed to be non-dispersive. These waves were first evident in the cloud deck near 30°S, 85°W during a 24 h period beginning at midday on 7 October 2008, and propagated northeastward toward the Peruvian coast for the following 48 h. During this time they induced both reversible and non-reversible changes in cloud-radiative and cloud-dynamic properties, such that areas of clear sky developed in the troughs of passing wave-fronts. These pockets of open cells persisted long after the passage of the gravity waves, advecting northwestward with the background wind. Using the analysis fields of the European Centre for Medium-Range Weather Forecasts in conjunction with infrared and microwave satellite imagery, we show that these gravity waves emerged from a disturbed subtropical jet stream. The radiant of the waves was coincident in all cases with centres of large negative residuals in nonlinear balance, suggesting that geostrophic readjustment of sharply divergent flows associated with the disturbed jet provided a source for the wave energy. Conversely, gravity waves were not observed in more quiescent jet conditions. This case study highlights the important and irreversible effects that gravity waves propagating in the troposphere can have on cloud radiative properties (and hence surface radiation budgets) over a very wide area. It also highlights the importance of synoptic influence on Sc-covered marine boundary layers. Copyright © 2012 Royal Meteorological Society

Key Words: VOCALS; stratocumulus; gravity waves; pockets of open cells; cloud microphysics; scale interactions

Received 2 September 2011; Revised 13 March 2012; Accepted 20 March 2012; Published online in Wiley Online Library

Citation: Allen G, Vaughan G, Toniazzo T, Coe H, Connolly P, Yuter SE, Burleyson CD, Minnis P, Ayers JK. 2012. Gravity-wave-induced perturbations in marine stratocumulus. *Q. J. R. Meteorol. Soc.* DOI:10.1002/qj.1952

1. Introduction

The extensive stratocumulus (Sc) sheets found in the subtropics on the eastern sides of the Pacific and Atlantic oceanic basins play an important role in the Earth's radiation budget through their high reflectivity. According to the Intergovernmental Panel on Climate Change, predicting how these, and other low clouds, will evolve in the changing climate of the coming centuries is one of the largest sources of uncertainty in current climate models (e.g. Randall *et al.*, 2007; Meehl *et al.*, 2007). One of the distinctive features of the Sc sheets that cannot be reproduced in such models is the extensive dynamical variability, exemplified by the opening up of pockets of open cells (POCs) in otherwise unbroken boundary-layer cloud (characterized further by Stevens *et al.*, 2005). Understanding the physics of these POCs was one of the main objectives of the VOCALS experiment (see section 2.1) conducted in the southeast Pacific in the (southern) spring of 2008. Here we report on a possible trigger for the formation of these features by atmospheric gravity waves propagating across the domain of the cloud sheet. This article also shows how reversible dynamical perturbations caused by gravity waves can result in irreversible changes in the cloud field through their interaction with the cloud microphysics.

The processes responsible for POC formation are believed to involve a coupling between cloud microphysics, aerosols and boundary-layer dynamics (e.g. Bretherton *et al.*, 2004; Comstock *et al.*, 2005; Stevens *et al.*, 2005; Petters *et al.*, 2006; Wood *et al.*, 2008, 2011a; and references therein). Very briefly, local dynamical processes leading to enhanced drizzle formation in Sc clouds remove moisture and cloud condensation nuclei (CCN) from the boundary layer, thus suppressing recovery of the cloud from the moisture sink of drizzle. A range of both modelling (e.g. Wang *et al.*, 2010) and observational case studies (Stevens *et al.*, 2005; Comstock *et al.*, 2007; Wood *et al.*, 2011a) of marine Sc have now linked the formation of POCs with the presence of drizzle in a CCN-poor environment. Ship observations during VOCALS-REx (see section 2.1) consistently showed more intense clouds and drizzle and higher liquid water path (LWP) when cloud tops where higher (deSzoeke *et al.*, 2010). In a modelling study of the area near 20°S, 85°W, where strong drizzle was observed during VOCALS, Mechem *et al.* (2012) found that an increase in the boundary layer height of 200 m yielded a greater change in drizzle intensity than halving CCN concentration from 270 cm^{-3} to 135 cm^{-3}. When the cloud passes a critical (as yet uncharacterized) threshold in terms of CCN concentration and bulk properties such as liquid water content, it dissipates and responds dynamically by switching from closed cellular to open cellular convection, with the remaining cloud limited to the ascending branches of the open cells. However, it must be noted that the processes and interactions leading up to the formation of drizzle may be manifold, i.e. thermodynamic or CCN-driven, and as such, the ultimate causes of POC formation may be equally diverse.

The hypothesis being examined here is that a gravity wave imposes a periodic pattern of vertical motion on the cloud deck, alternately lifting and lowering it. As the cloud is lifted it thickens and cools, causing drizzle to form which washes out moisture and CCN. In the opposite phase of the wave the cloud warms and dissipates, creating a hole. When the wave has passed, this hole is left behind as a nascent POC.

Although earlier studies have demonstrated a potential coupling between tropospheric gravity wave generation and relatively short-lived cloud formation (lasting a few hours at most) through dynamical arguments alone (e.g. Haag and Karcher., 2004; Knippertz *et al.*, 2010), the process discussed in this study suggests a hitherto unidentified role for gravity waves through both long-range and long-lived influences on tropospheric cloud. Furthermore, this study suggests a coupling to irreversible microphysical processes, which, under appropriate conditions, may lead to cloud dissipation, with consequences for the tropospheric energy budget and hence climate.

In this article we will examine satellite imagery and thermodynamic fields for October 2008, focusing in specific detail on the period 7–9 October, when gravity waves were observed to have the most pronounced impacts on cloud properties. We will then discuss two other episodes of gravity wave propagation that reveal a common source mechanism. We have not examined potential events beyond October and November 2008 and therefore cannot determine the climatological significance of this phenomenon – though we note that such a study is required for the climate community to place the focused observational study we present here in context. We now briefly describe the field project that was active at the time of the case study and describe our data sources before continuing to discuss satellite and thermodynamic observations.

2. The VOCALS campaign and data sources

2.1. The VOCALS-REx Campaign

The events discussed here were observed immediately prior to the intensive phase of the Variability in the American Monsoon System (VAMOS) Ocean–Cloud–Atmosphere–Land Study Regional Experiment (VOCALS-REx) field campaign, and we make use of satellite data generated in support of this international multiplatform campaign. A key objective of VOCALS-REx was to reduce uncertainties in current and future climate projections; especially those associated with marine Sc and coupled land–ocean–atmosphere processes. The field campaign consisted of the following measurement platforms: five aircraft, two cruise ships, two surface measurement sites and data from two IMET Buoys (positioned at 20°S, 85°W and 20°S, 75°W) as well as a host of supporting satellite data and specialist model output to inform mission planning in the field. Further details of the context, platforms and instrumentation operated during VOCALS-REx can be found in Wood *et al.* (2011b), Allen *et al.* (2011) and Bretherton *et al.* (2010).

2.2. Satellite datasets

Satellite measurements provide a practical method for observing marine Sc and cloud bulk properties over the remote open ocean. In this study, we make use of visible, infrared and microwave satellite spectroradiometers, which include the 10th Geostationary Operational Environmental Satellite (GOES-10); and the MODerate-resolution Spectroradiometer (MODIS) and Advanced Microwave Sounding Radiometer-EOS (AMSR-E) on NASA's polar-orbiting Aqua satellite

The GOES-10 geostationary weather satellite, jointly operated by NOAA and NASA, routinely provided infrared and visible images of the South American region from 1997 until its decommissioning in 2009 (see Menzel and Purdom (1994) for further technical details). The GOES-10 recorded images at 4 km resolution in five spectral bands, including a visible, short-wave infrared and three thermal infrared channels. For this work we use half-hourly brightness temperatures recorded in the GOES-10 infrared window (IRW) channel 4 (10.8 μm) to illustrate the propagation of gravity waves. This mid-infrared channel is chosen to limit sensitivity to changes in cloud-top radiance inherent to the diurnal cycle. Brightness temperature perturbations are used as a proxy for changes in cloud-top temperature and hence cloud-top height. In addition, cloud properties were retrieved from GOES-10 imagery at half-hourly intervals, using the visible infrared solar-infrared split window technique (VISST) and the solar-infrared split window technique (SIST) methods described by Minnis *et al.* (2011). These methods use GOES-10 brightness temperatures in four channels during daytime (VISST) and three during night-time (SIST) in conjunction with other available satellite and meteorological observations to derive information on cloud-top height (CTH), LWP and other bulk cloud quantities. Cloud-top height is defined as the point of least difference between cloud-top temperature and a co-located European Centre for Medium-Range Weather Forecasts' (ECMWF) reanalysis temperature profile.

Data from both the MODIS and AMSR-E sensors are used here to detect strong drizzle. Drizzle forming in the presence of the gravity waves (see section 3) is identified using a novel technique (Miller, 2010). There were 11 Aqua overpasses of the southeast Pacific (SEP) region between 7 and 10 October 2008, occurring approximately half an hour after local noon and midnight.

In clouds without ice, such as the marine Sc in the southeast Pacific, strong drizzle (LWP > 200 g m^{-2}) manifests as small patches of higher microwave brightness temperatures when contrasted with the smoother background emission from the ocean surface and water vapour. The 89 GHz brightness temperatures of the AMSR-E are used to detect drizzle at the native resolution of the sensor (4 km $\times$6 km), which is sufficient to identify larger regions of strong drizzle. The method works only in regions without mixed phase or ice clouds and where the drizzle is strong. Hence, this technique is well suited for this study, where most often only Sc clouds appear in the field-of-view over the southeast Pacific.

2.3. *Reanalysis data of the ECMWF*

For synoptic meteorological analysis, we use operational analysis fields produced by the ECMWF Integrated Forecasting System (IFS Cycle 29r2) on a $2.5° \times 2.5°$ geospatial grid on 91 hybrid model levels. Derived variables such as potential vorticity are calculated explicitly here from base thermodynamic fields (pressure, temperature, specific humidity and three-dimensional winds).

In addition, for the purposes of this study, we will use base thermodynamic fields to diagnose a spatially gridded residual to the nonlinear balance equation (NBE) as a proxy for regions of unbalanced flow associated with large curvature in high amplitude Rossby waves, which were known to be prevalent over the southeast Pacific in October 2008 (Toniazzo *et al.*, 2011). The residual to the NBE is defined as (e.g. Zdunokowski and Bott, 2003, p. 450):

$$\Delta NBE = 2J(u,v) + f\zeta - \nabla^2\Phi - \beta u, \qquad (1)$$

where f is the Coriolis frequency, $\beta = df/dy$, ζ is relative vorticity, Φ is geopotential height and the Jacobian term, $J(u,v) = (\mathrm{d}u/\mathrm{d}x \cdot \mathrm{d}v/\mathrm{d}y) - (\mathrm{d}v/\mathrm{d}x \cdot \mathrm{d}u/\mathrm{d}y)$. The NBE is obtained through scale analysis of the divergence equation by dropping all terms containing the divergence and the vertical velocity. A non-zero sum of the terms of the right-hand side of Eq. (1) has been shown previously to represent flow imbalance associated with strong divergence seen in rawinsonde data (Moore and Abeling, 1988) and has also been employed with mesoscale model fields for the purpose of analysing the degree of flow imbalance. Most importantly, in those studies (Zack and Kaplan, 1987; Koch and O'Handley, 1997; Koch *et al.*, 1998; Zhang *et al.*, 2001) a region of large NBE residual was found to occur within the generation region of gravity waves.

3. Observations from satellite imagery between 7 and 9 October 2008

We now focus on the period 7–9 October 2008 when gravity waves were observed to cause the largest modulation of cloud-top height over the southeast Pacific within our period of study (October and November 2008). Figure 1 shows a time sequence (at 4 h intervals) of GOES-10 IRW brightness temperature maps grey-scaled within the range 278–282 K for a period between 05:45 local time (0845 UTC) on 8 October 2008 and 13:45 local time (1645 UTC) on 9 October 2008. In addition, a full animated sequence of GOES IRW brightness temperature imagery across October 2008 is provided as a supplement to this article and we strongly recommend that the reader view this to facilitate understanding of this dynamic phenomenon, which can be conveyed only in a limited way in the still imagery within this article. Bright areas on this scale indicate cooler brightness temperatures representative of higher cloud top and vice versa. The warmer sea surface, and hence cloud-free, regions appear black on this scale. The sequence shows several parallel wave-fronts superimposed on the brightness temperature field, evident as light and dark bands aligned roughly in a northwest–southeast direction between 90°W to 80°W and 23°S to 27°S. White boxes in Figure 1 highlight the wave-fronts. Magnified images of the areas within these highlighted boxes are shown in Figure 2 with an approximate spatial scale (assuming a Great Circle distance at 20°S) and serve to better illustrate the individual wave-fronts and their structure. The sequence shows that the wave-front seen in Figure 1(a) advanced toward the northeast and was the first wave-front of a wave train. A more detailed tracing of each wave-front from a full sequence of GOES-10 imagery reveals that the peak of each wave-front propagated at a phase speed of approximately 55 km h^{-1} (15.3 m s^{-1}) across the domain. Furthermore, analysis of the interarrival time between these fronts at a fixed location yields a wave period of approximately 60 min and hence a wavelength of 55 km.

An important additional observation is that the waves were non-dispersive: there was no evidence of wave-fronts propagating within a broader envelope moving at a different velocity. This is to say that the observed phase speed

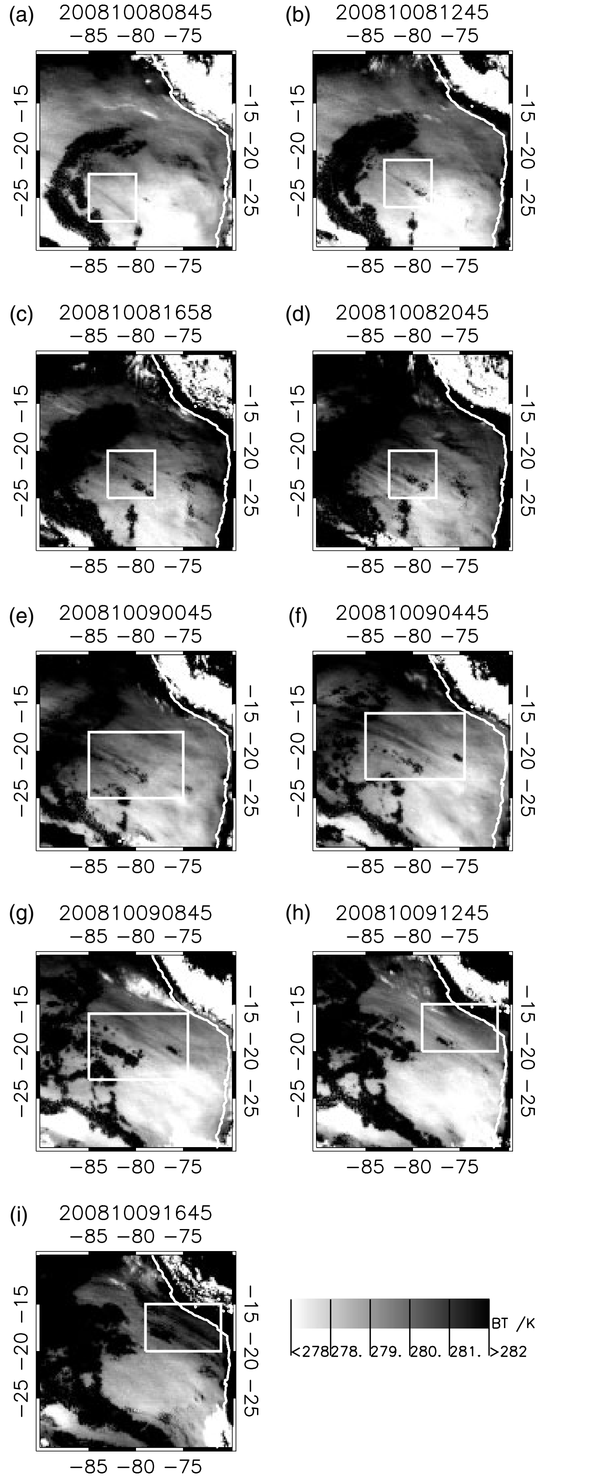

Figure 1. Time sequence at approximately 4 h intervals (see time labels for each panel) of GOES-10 thermal infrared window brightness temperature (greyscaled within the range 278–282 K) across the period 0845 UTC, 8 October 2008 to 1645 UTC, 09 October 2008. The sequence shows the progression of a gravity wave-front highlighted within the white box on each panel.

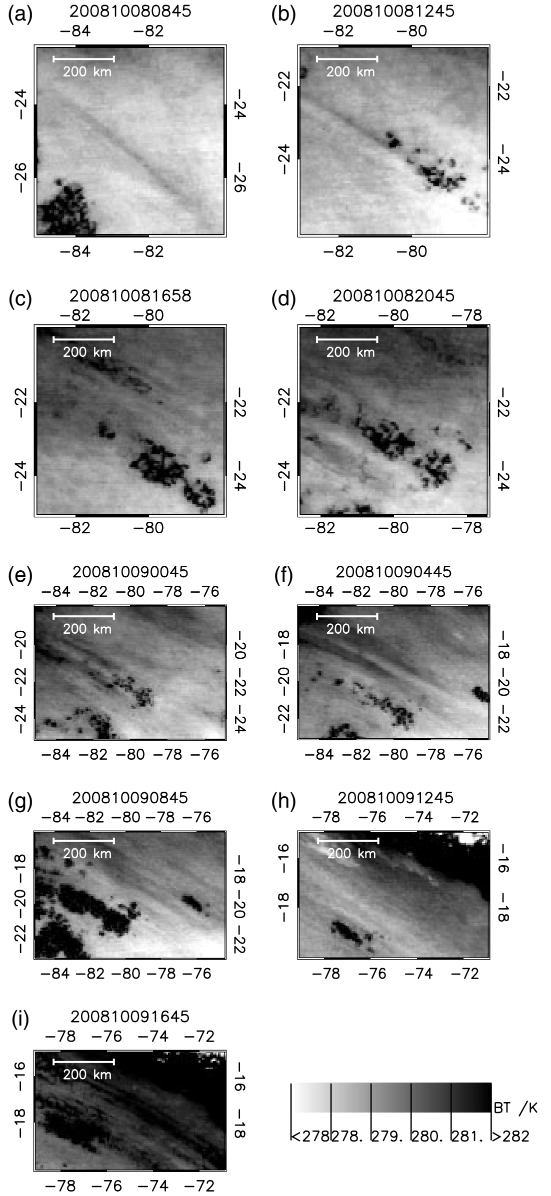

Figure 2. Magnified images of the time sequence (see time labels for each panel) of GOES-10 IRW brightness temperatures across the period 0845 UTC, 8 October 2008 to 1645 UTC, 9 October 2008, presented in Figure 1.

and group speed were equal, which, as we argue below, has implications for the vertical structure of the waves. Figures 1(f)–(i) and 2(f)–(i) show the sequence between 0445 UTC and 1645 UTC on 9 October, which completes the life cycle of the waves as they finally reach the Peruvian Coast at approximately 1645 UTC. We see that the POC feature seen clearly as the mostly cloud-free area embedded in the Sc field in Figure 1(d), continues its northwestward advection in the mean flow and continues to separate from the gravity wave train. By the end of the sequence, the POC feature, originally initiated well to the southeast, had persisted for 28 h before entering a more general cloud-free area to the west (in the transition region to trade cumulus outside of the Walker anticyclone). A composite schematic of the time and location of the foremost wave-front observed in the GOES-10 imagery in Figure 1(a) is presented in Figure 3.

The light and dark banding in brightness temperatures seen in Figures 1 and 2 can be thought of qualitatively as minima and maxima in cloud-top temperature and hence peaks and troughs in CTH, respectively. Where solar zenith angle permitted GOES-10 CTH retrievals, the maximum peak-to-trough difference in CTH was found to be 400 m as calculated between maximal and minimal pixels (see Figure 4). These perturbations were seen around a mean background CTH of ∼1300 m at 20°S, 76°W

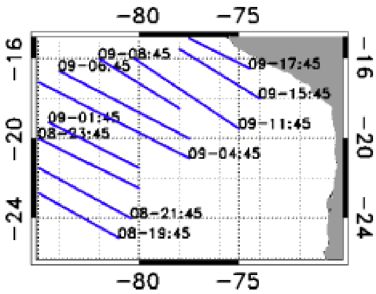

Figure 3. A composite schematic showing the position and extent of gravity wave-fronts (in blue) in the southeast Pacific as observed in GOES-10 imagery. The label for each wavefront gives the day in October 2008 followed by Universal Time. This figure is available in colour online at wileyonlinelibrary.com/journal/qj

(Figure 4(b)). Average peak-to-trough differences in CTH calculated along the wave-fronts as a whole were typically much less than this (between 100 and 300 m). These periodic undulations in CTH also propagated almost perpendicular to the mean boundary layer flow (diagnosed from the ECMWF horizontal boundary layer wind field). This is observed in Figure 1 and in the accompanying movie sequence by the separation of the POC features from the advancing gravity wave-fronts. The sequence in Figure 1 shows that in a 32 h period, the wave-fronts propagated across approximately 10° of longitude and 8° of latitude over the southeast Pacific northeastward toward the coast of Peru. The nature of this periodic, crossflow-propagating disturbance, the phase speed and horizontal wavelength all point to a mesoscale gravity wave that was initiated to the southwest and travelled across the domain. We note that at the southernmost end of the domain the wave signature could also be seen in cirrus clouds, showing that the gravity wave was present throughout the troposphere. A false-colour image of brightness temperature tuned for cirrus is presented in Figure 5. In this figure, we see a thin band of cirrus propagating over a 1.5 h period beginning at 0828 UTC on 9 October 2008. The cirrus band is also aligned in a southeast–northwest direction and calculations of phase speed and period for the band seen across Figure 5 reveal values (phase speed 16.5 m s^{-1}, period 59 km) similar to the wave train observed a little to the north in the Sc deck below. This consistency between upper and lower levels of the troposphere suggests an atmospheric disturbance and hence a source a source of gravity wave energy that is rooted above the MBL inversion layer.

Figure 6 shows the LWP retrieved from GOES-10 radiances during the period of interest, magnified within the same regions highlighted in Figure 1 for corresponding times. It should be noted that accurate LWP estimates are not possible for high solar zenith angles (> 72°) due to the difficulty in accurately retrieving cloud effective radius, which requires information from near-infrared channels and hence sunlight. We therefore present only those LWP fields that were retrieved in daylight hours. We see a characteristic increase in background LWP with distance offshore from the South American coast (when comparing Figure 6(a) with Figure 6(c)), a consistent feature described by George and Wood (2010; and references therein). These LWP changes are probably a result of the increasing depth of the boundary layer and changes in its structure further offshore (Bretherton *et al.*, 2010). There is also a decreasing gradient in cloud droplet number away from the coast

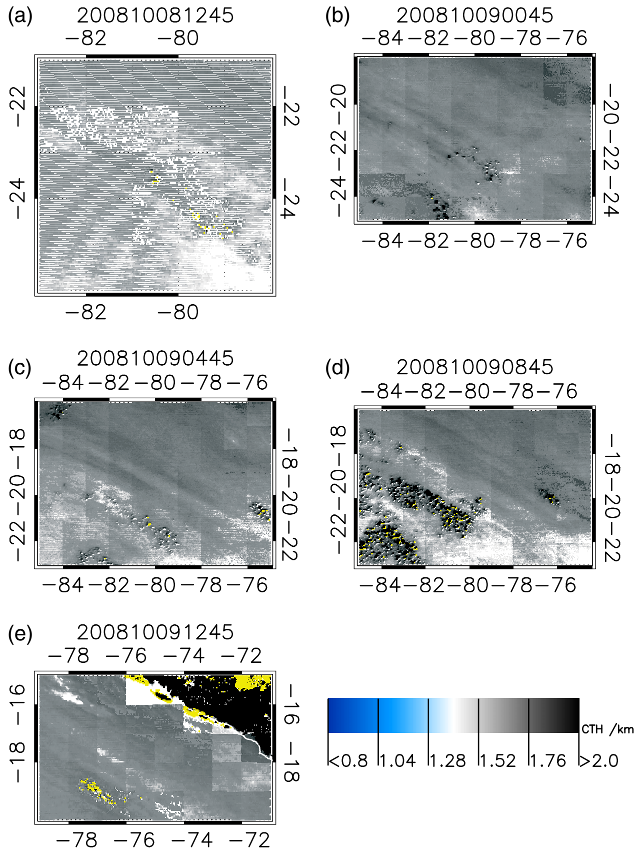

Figure 4. Time sequence (see time labels for each panel) of selected GOES-10 IRW-retrieved cloud top height (CTH) as indicated by the greyscale bar across the period 2345 UTC, 8 October 2008 to 1045 UTC, 10 October 2008. This figure is available in colour online at wileyonlinelibrary.com/journal/qj

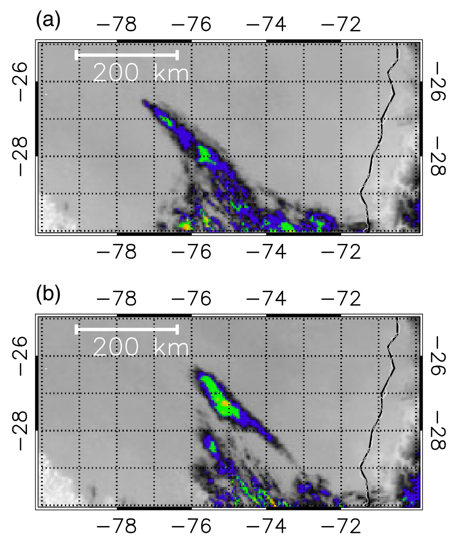

Figure 5. Cloud brightness temperature field retrieved from GOES-10 radiances in the region 30°S to 25°S, 80°W to 70°W and colour-scaled as indicated for (a) 0828 UTC and (b) 0958 UTC, on 9 October 2008. This figure is available in colour online at wileyonlinelibrary.com/journal/qj

which is associated with atmospheric composition in the local marine boundary layer, in particular the presence (or absence) of submicron aerosol which act as CCN (Allen *et al.*, 2011). Rain rate in Sc has been empirically observed to be proportional to the ratio of cloud LWP and droplet number (e.g. ship-based measurements reported by Comstock *et al.*, 2005), meaning that rain rate increases with increasing LWP

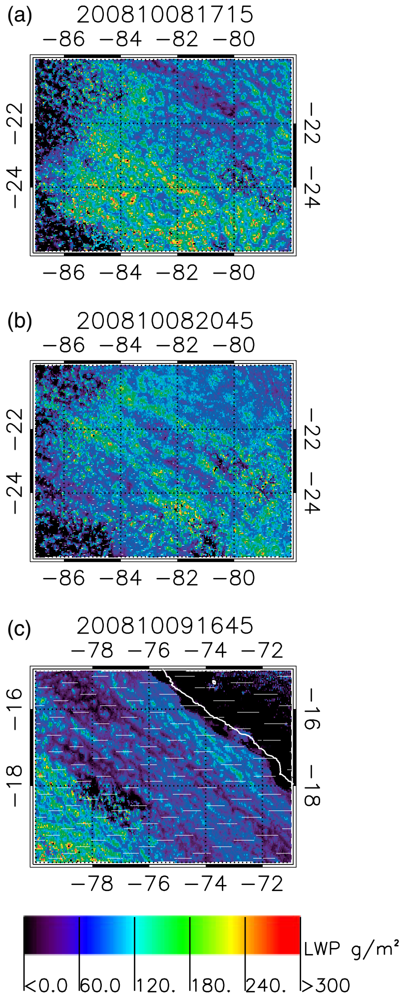

Figure 6. Time sequence (see time labels for each panel) retrieved from GOES-10 of liquid water path (LWP) as scaled. The LWP retrievals from GOES-10 are presented during daylight hours only (see text). This figure is available in colour online at wileyonlinelibrary.com/journal/qj

and decreasing droplet number. This relationship implies that there are both anthropogenic and natural influences on the observed precipitation rates across the region. Finer-scale variability in LWP in the southeast Pacific has also been correlated with both precipitation and CCN number, with local increases in LWP, particularly in the remote marine environment, being coincident with areas of strong drizzle and low CCN (Zuidema *et al.*, 2005). From those measurements and known relationships, we can conclude that Sc clouds observed to contain relatively high LWP in the remote marine environment are more frequently precipitating than those with lower LWP near to shore.

Figure 6(a) shows the crests of the gravity wave train at 1715 UTC on 8 October 2008 discussed earlier and corresponding to Figures 1(c) and 2(c). Wave peaks are seen here as an increase in LWP relative to the background. The LWP along the wave-fronts in Figure 6(a) is maximally around 200 g m^{-2}, with averages along the wave-fronts of around 150 g m^{-2}. This compares with a background of around 80 g m^{-2} in the background remote marine environment. Three and half hours later, in Figure 6(b), we can see that the wave train has advanced to the northeast and that a large area of generally enhanced LWP has developed as several more waves pass through the region. It is important to note that we expect a significant diurnal modulation in LWP and therefore the enhancements seen here should be interpreted in the context of the contrast between the wave crests and the instantaneous background. With this in mind, it is clear that the passing waves do enhance LWP relative to the unperturbed background. Furthermore, in Figure 6(b) we see the area of POCs corresponding to those observed in Figure 1(d) is seen here as areas of zero LWP embedded in the region of wave-enhanced LWP.

As discussed in section 1, POCs are known to be associated with strongly drizzling Sc cloud, and hence enhanced LWP, relative to non-precipitating cloud in an otherwise similar airmass. Figure 7 shows LWP and detected drizzle cells retrieved from MODIS and AMSR-E overpasses using the method described in section 2.2. An AMSR-E scene immediately prior to the gravity wave event (0540 UTC on 7 October 2008, Figure 7(a) is included for illustration of the typical background environment, which shows an absence of significant drizzle across the region, with the exception of a small region of POCs near 24°S, 81°W. After analysis of all microwave satellite instrument overpasses during the period of interest, only two overpasses of the region of interest were sampled by AMSR-E, at 1845 UTC on 8 October 2008 (Figure 7(b)) and 0528 UTC on 9 October 2008 (Figure 7(c)), corresponding most closely with the GOES-10 imagery shown in Figures 1(c) and 2(c); and Figures 1(f) and 2(f), respectively. The AMSR-E LWP fields complement the GOES-10 LWP fields presented in Figure 6. Figures 7(b) and 7(c) demonstrate that the wave crests seen at 18°S, 77°W in Figures 1(c) and 1(f) did indeed induce precipitation at the same locations sampled by AMSR-E – seen as the dark bands in the right-hand panels of Figures 7(b) and 7(c). In addition to influences on Sc cloud far offshore, there were also some noteworthy changes in the cloud field when the gravity wave train reached the near-shore environment, as seen in terms of brightness temperature in Figures 1(i) and 2(i), and in terms of satellite LWP in Figures 6(c) and 7(c). In particular, a large area of POCs located just to the south of a sharp gradient in LWP at around 18°S, 77°W (see Figures 1(i) and 2(i)), rapidly developed as the wave-fronts passed through (see movie sequence). The sharp gradient defines a natural boundary between the relatively clean maritime air and the more polluted coastal aerosol regime, bounded by the synoptic coastal jet – a dynamical feature associated with the Andes topography (see Rahn *et al.*, 2011). Further linear bands of cloud clearance were also observed nearer to the coast. The reason for the rapid development of a POC feature at this location is unknown although we speculate that this could be due to a complex interaction between the propagating wave train and the coastal jet, which may be further underpinned by the rapid change in the aerosol regime. A detailed examination of this process is beyond the scope of this article and we concentrate hereon on the more readily characterized remote marine environment.

4. Conceptual model and microphysical process interactions

The enhancement of LWP and the initiation of drizzle in the remote marine environment are critical to an understanding of the proposed microphysical process linking gravity wave propagation with POC formation. As a gravity wave passes through an area, alternating regions of induced convergence and divergence in alternate phases of the wave result

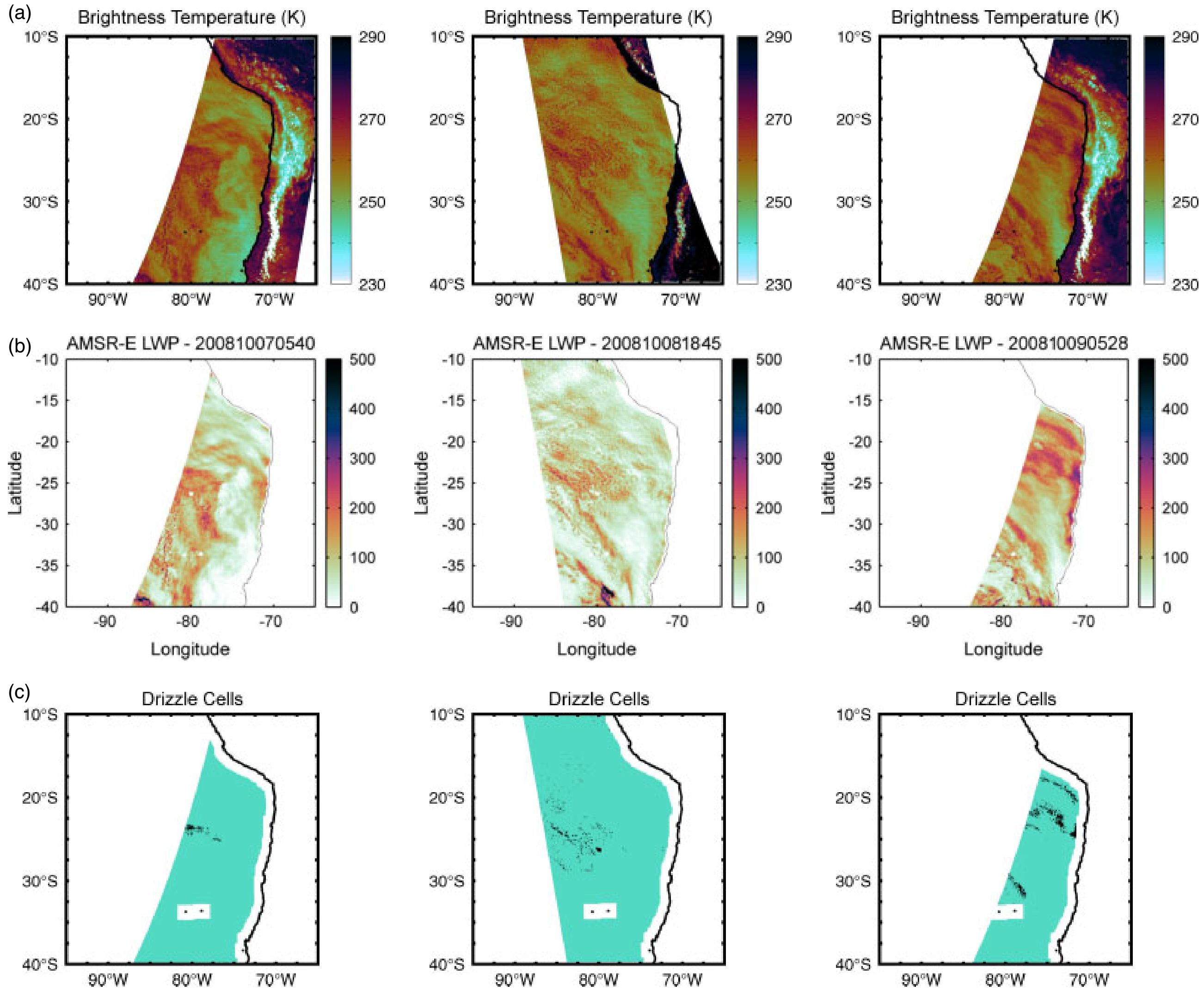

Figure 7. Brightness temperature swaths (left panels), liquid water path (centre panels) and strong drizzle (black cells in right panels) retrieved at 89 GHz from AMSR-E overpasses, at: (a) 0540 UTC, 7 October 2008; b)1845 UTC, 8 October 2008; and c) 0528 UTC 9 October 2008. Note: The black dots inside white squares near 33°S, 88 W, in the right panels are two islands, which are masked for the purposes of the drizzle retrieval algorithm. This figure is available in colour online at wileyonlinelibrary.com/journal/qj

in corresponding regions of net ascent and descent. In regions of ascent (positive phase of the passing wave), a rapid drop in temperature throughout the cloud layer results in additional condensation of water vapour. This water vapour condenses onto existing cloud droplets and may form new cloud droplets (subject to availability of CCN), hence increasing cloud LWP. This is consistent with the pattern seen in satellite observations in Figures 6 and 7 discussed earlier. In this remote maritime region characterized by low CCN concentrations (Bretherton *et al.*, 2010; Allen *et al.*, 2011), any additional condensation will result in a shift to larger mean droplet size (due to both condensation onto existing droplets and greater collisional coalescence efficiency) and some of those droplets may become precipitable. Importantly, the LWP observed along the wave-fronts in Figure 5(a) ($100-140\ \mathrm{g\,m^{-2}}$) is consistent with values found in strongly drizzling Sc in the remote southeastern Pacific (Zuidema *et al.*, 2005) and the detection of co-located drizzle by AMSR-E (see Figure 7(b)) confirms this. This leads to loss of water from the cloud. As the wave passes into the negative phase (downward movement of the cloud) and the local temperature rises, the remaining cloud will contain less liquid water than before, and may even evaporate altogether if the wave perturbation is sufficiently large. The period of the observed waves (around 1 h) is similar to the boundary-layer eddy turnover time-scale (typically an hour or less, Wood, 2012) and therefore the resupply of moisture to the cloud layer is not fast enough to offset the loss of cloud liquid water by precipitation.

Together, removal of cloud liquid water by precipitation in the upward phase and subsequent adiabatic cloud droplet evaporation in the downward phase, could be expected to lead to large reductions in total water content and hence cloud clearance. Both the near-LES simulations of Mechem *et al.* (2012) and a simple parcel model using observed modulation of CTH and ECMWF thermodynamic profiles have demonstrated that this is indeed possible over the area, and is confirmed here by the GOES-10 satellite observations. For example, consider the following simple adiabatic thermodynamic calculations for a cloudy air parcel, which is lifted by 100 m (the observed typical average amplitude of the waves) and 200 m (the observed maximum amplitude seen in Figure 4). Assuming typical aircraft profiles of cloud microphysical parameters (liquid water content, cloud top temperature and droplet number concentration) and thermodynamic profiles obtained later

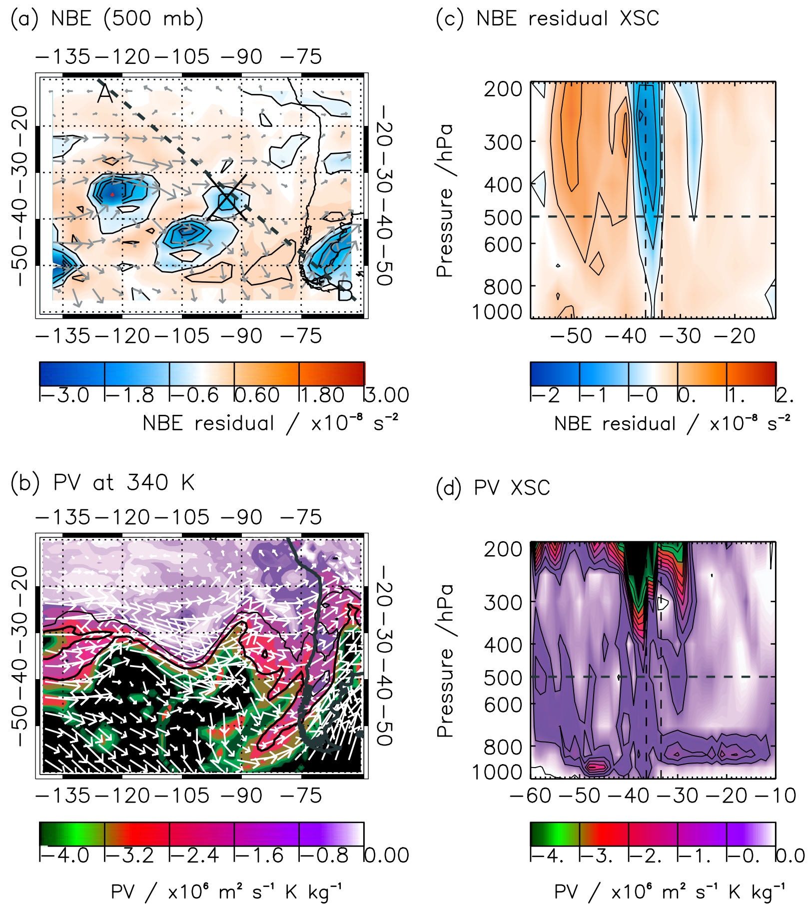

Figure 8. Thermodynamic operational analysis and derived fields from the ECMWF IFS at 1200 UTC on 6 October 2008 for: (a) residual of the NBE (colour-scale) and scaled horizontal winds (grey arrows) evaluated at 500 hPa; (b) potential vorticity (colour-scale) evaluated on the 340 K isentropic surface with scaled horizontal wind arrows (white); (c) Vertical–horizontal cross-section of residual of NBE, extracted along the dashed line marked between AB on (a); and (d) cross-section of potential vorticity along the same line. The abscissa in (c) and (d) is the latitude along the cross-section. The cross in (a) marks the mid-point of the gravity wave packet observed at 0845 UTC on 8 October 2008, projected back in time to 1200 UTC on 6 October using the measured phase speed. The dashed lines on (c) represent a line along the 500 hPa level (for reference to (a)) and the latitudinal range of the back-projected wave-front, respectively. This figure is available in colour online at wileyonlinelibrary.com/journal/qj

in VOCALS-REx (described by Allen *et al.*, 2011), uplift of 100 m corresponds to an additional condensation of 0.15 g m^{-3} of water vapour, increasing to 0.3 g m^{-3} for 200 m uplift (assuming a theoretically derived moist adiabatic lapse rate of 1.5 g m^{-3} km), If we assume that the initial liquid water content of the unperturbed cloud is ∼0.6 g m^{-3} and cloud droplet concentration was 100 cm^{-3} (in line with *in situ* measurements in remote Sc reported in Bretherton *et al.*, 2010) then the mean droplet diameter initially would be ∼22.5 μm by the following relationship for a cloudy air parcel taken from Miles *et al.* (2000):

$$\overline{D} = \sqrt[3]{\frac{LWC}{N_d \frac{\pi}{6} \rho_w}}, \qquad (2)$$

where D is the mean droplet diameter, LWC is the liquid water content, N_d is the cloud droplet number and ρ_w is the density of liquid water. With the additional condensation induced by the wave uplift of 100 m, then by Eq. (2), the mean droplet size in cloud at the crest of the gravity wave would be ∼24.2 μm, increasing to 25.8 μm for a 200 m uplift. This increase in mean droplet size may promote the development of precipitable droplets by increased collision and coalescence efficiency and the size calculated for 200 m uplift is consistent with cloud-top mean droplet sizes observed in drizzling marine Sc (e.g. Bott, 1998). This leads to the suggestion that the observed gravity waves may not always be expected to induce drizzle and only those lifting cloud by the upper range of that observed may lead to precipitation. This is precisely what we observe in Figure 7 – that not all gravity waves leave drizzling cells or clear air in their wake. Furthermore, the natural range of thermodynamic variability of the Sc cloud deck across the southeast Pacific region as a whole may mean that some clouds are more sensitive to small changes than others in terms of promoting precipitation. In saying this we must also recognize the limitations of the above adiabatic assumption; the true response of cloud to gravity-wave-induced perturbations is likely to be a function of many coupled and non-linear processes (e.g. changes in long-wave cooling at cloud top). Therefore a full examination of the likely sensitivities is beyond the scope of this work and would benefit from tailored cloud modelling studies at the large eddy scale. Such a study is now underway by the authors.

We propose here, based on these observations, that gravity waves are able to initiate drizzle and tip clouds in a predisposed region (of low CCN) into the POC state, shown in the satellite imagery here as an 'opening up' of the cloud deck in lines parallel to the phase fronts. An investigation of this process using a cloud-resolving model is the subject of an ongoing study.

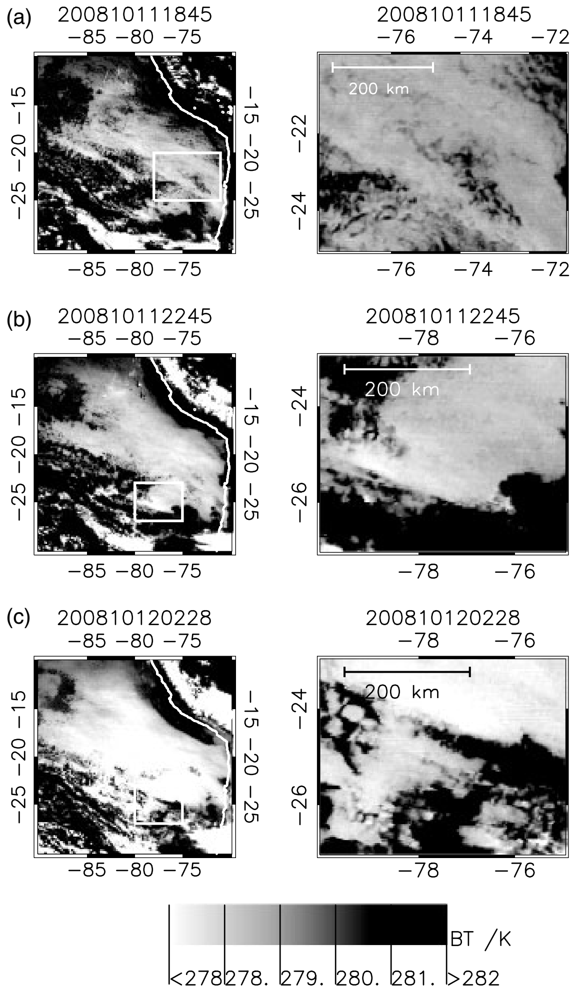

Figure 9. Time sequence at approximately 4 h intervals (see time labels for each panel) of GOES-10 thermal infrared window brightness temperature (greyscaled within the range 278–282 K) across the period 1845 UTC, 11 October 2008 to 0228 UTC, 12 October 2008. The sequence shows a series of gravity waves highlighted within the white box on each left panel, with the corresponding zoomed area in the right panels.

A summary of the satellite observations in section 3 is that the wave-fronts shown here propagated for a period of over 32 h and over a distance in excess of 1500 km, suggesting trapping of wave energy in the troposphere. Having established the changes in observed cloud bulk properties and the microphysical processes that might lead to observed irreversible changes in cloud dynamics at the mesoscale, we now investigate the source of the gravity waves and briefly discuss the possible reasons for trapping.

5. Sources of gravity wave energy in October 2008

Mesoscale trains of atmospheric gravity waves have been reported many times in the literature, with properties similar to those described here (e.g. Bosart *et al.*, 1998). Often, they have been associated with deep convection, but Uccellini and Koch (1987) who presented a summary of 13 published case studies of such waves, decided that convection was not their main source of energy. They concluded that a common feature in all such events was a jet streak upstream of an upper-level ridge, with the waves found 'in the exit region of a jet streak and preferentially on its right (anticyclonic shear) side'. Uccellini and Koch were not able to explain the precise mechanism for wave emission, but they suggested shear instability and geostrophic adjustment as the two most likely mechanisms: in the exit region of the jet streak strong departures from nonlinear balance are found, which can cause the emission of gravity waves by geostrophic adjustment. Zhang *et al.* (2001, 2003) examined this hypothesis in detail for a gravity wave case reported by Bosart *et al.* (1998), using a simulation of the event with the MM5 mesoscale model. In this case wave initiation occurred just downstream from a region of nonlinear imbalance, itself downstream of an upper-level trough over the eastern USA. The largest departure from nonlinear balance was found in the tropopause fold beneath the southwesterly branch of the jet stream. The waves generated at upper levels took several hours to reach the surface layer and resulted in one long-lived, large-amplitude gravity wave train that caused hazardous winter weather.

We shall now discuss sources for the wave energy, dealing first with the observational case already presented in section 3 and then with two other cases observed later in October 2008.

5.1. 8 October 2008 case

For the case discussed in section 3, the wave-fronts were first observed near 30°S, 85°W on the afternoon of 7 October 2008. Using the phase speed of the (non-dispersive) waves as derived in section 3 from their track on the cloud field (see Figure 3) and assuming a constant speed and direction we are able to approximately trace back the waves from their initial point of observation in order to diagnose the potential original imbalances that may have acted as a source for the wave energy. Figure 8 shows fields derived from ECMWF operational thermodynamic analyses at 1200 UTC on 6 October 2008 (around 36 h before the waves were first manifest as perturbations to the Sc cloud deck). Figure 8(a) shows ΔNBE, calculated as described in section 2.3, at 500 hPa along with the back-traced position of the gravity waves first observed in Figure 1(a), marked by a large cross. The dashed line between A and B in Figure 8(a) defines a line for which a vertical–horizontal cross-section parallel to the observed wave-front is extracted and plotted in Figures 8(c) and 8(d), for ΔNBE and potential vorticity, respectively. Figure 8(b) shows potential vorticity and horizontal winds on the 340 K isentrope, representative of the subtropical upper troposphere and extratropical lower stratosphere, therefore illustrating the position of the southern subtropical jet stream.

Figure 8(b) shows a markedly disturbed jet with three breaking Rossby waves between 140°W and 60°W. The point of interest here, corresponding to the black cross in Figure 8(a), is around 95°W, 36°S, just downwind from a ridge at 340 K. This breaking Rossby wave resulted in a tropopause fold, shown in Figure 8(d), which coincided with the large negative NBE residual vertical profile at 36°S (dark blue contours) seen in Figure 8(c) extending from 200 to 800 hPa. This large negative NBE residual results from convergence occurring in the equatorward branch of the jet stream downstream from the ridge, following the rapid increase in absolute vorticity along the flow. A fully animated sequence of the ECMWF fields displayed in Figure 8 across October 2008 is provided as a supplement to this article and illustrates more clearly the movement of the breaking Rossby waves across the SEP.

Temperature and humidity profiles from the ECMWF analyses along the path of the gravity wave trains showed

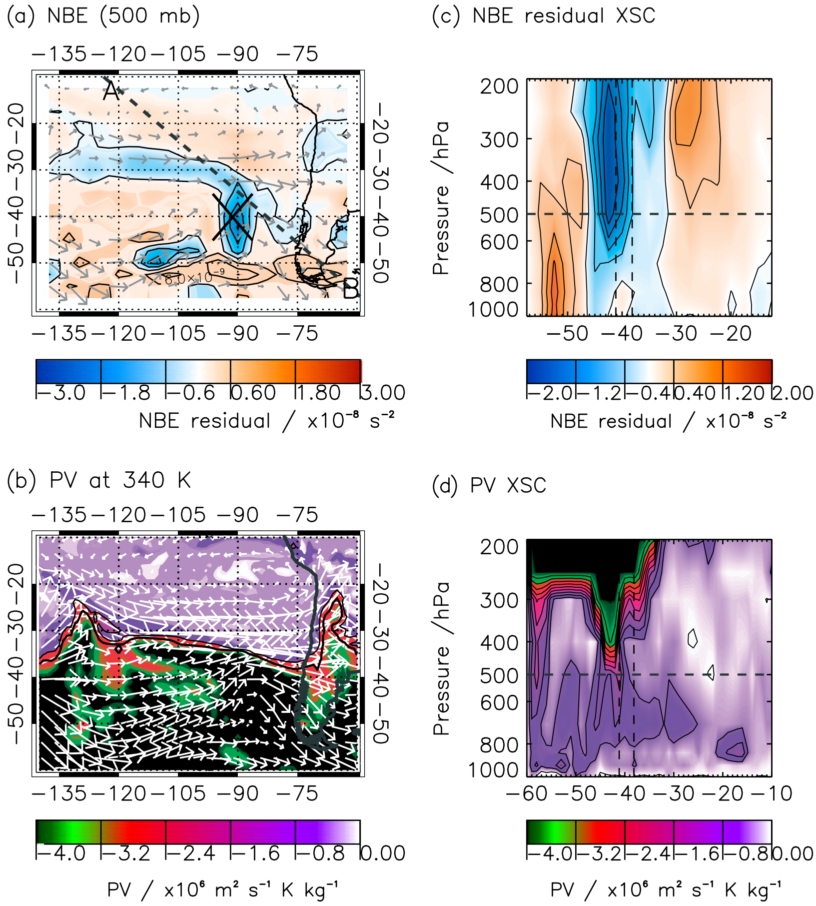

Figure 10. Same as Figure 8 for 0600 UTC on 10 October 2008, with the black cross in (a) marking the mid-point of the backward-traced gravity wave-front observed at 1528 UTC on 11 October 2008. This figure is available in colour online at wileyonlinelibrary.com/journal/qj

the boundary layer to be capped by a very prominent inversion ($\Delta\theta \sim 5$ K in 200 m). This layer was too thin to support the gravity waves observed here, which would have propagated into the stable layer above (Brunt-Vaisala frequency $N \sim 0.01$ s^{-1}). However, at the level of the inversion (or cloud top) the waves in fact propagated horizontally for around 2000 km without observable loss of amplitude. Linear, steady wave ducting by critical layers is one mechanism proposed in the literature for trapping gravity waves in the vertical (Lindzen and Tung, 1976). The non-dispersive nature of the waves would suggest a vertical wavelength of the order of 10 km. Indeed, there were critical layers in the upper troposphere along much of the path of the waves according to the ECMWF analyses, but the model static stability suggests that such layers would absorb rather than trap the wave energy. As we do not have detailed vertical profiles of static stability we cannot rule out the Lindzen and Tung mechanism here but it does not appear to be a strong candidate.

Short of some mechanism for reflecting the wave energy at the tropopause, we must consider the possibility that the observed undulations of the Sc deck are either a time-dependent wave with a complex, non-linear propagation, or result from a mechanism for wave amplification compensating for the propagation of wave energy upwards into the stratosphere. One such mechanism might arise from an interaction between the Sc deck and the wave, whereby subsidence across the inversion is affected by the vertical displacement associated with the wave.

The limited vertical resolution of the ECMWF analyses and the lack of *in situ* profiles in the region at this time preclude a detailed investigation of wave propagation. High-resolution model simulations are currently under way to determine whether the waves were predictable, given the large-scale flow pattern. The evidence in this section, however, clearly points to waves being generated by geostrophic adjustment around the subtropical jet stream, followed by horizontal propagation in the free troposphere for around 2000 km.

5.2. 11 October 2008 case

Having now demonstrated the existence of gravity waves and having described our conceptual model for the general process interactions from a detailed analysis of the 8 October 2008 event, we now describe two further events in October 2008 where gravity waves were observed on the Sc field in the same region. Figure 9 shows satellite imagery for propagating gravity waves observed in a sequence of selected GOES-10 thermal infrared images between 1845 UTC on 11 October 2008 and 0228 UTC on 12 October 2008 at 4 h intervals. For this case, we show the zoomed-out regions and zoomed-in regions side-by-side. Figure 9(a) shows a wave-front similarly aligned in a northwest–southeast direction and advancing to the northeast, centred at around 78°W, 23°S. Figures 9(b) and 9(c) show subsequent waves moving in the same direction.

The enhanced brightness of these clouds in the thermal infrared again demonstrates that the clouds have been lifted.

It is difficult to diagnose the presence of POCs induced by the waves in this more generally broken Sc field. However, the accompanying animation shows that the wave-front promotes cloud formation along the wave peaks as it moves northeastward in otherwise large cloud-free regions between 25°S and 20°S, 75°W to 80° W.

Figure 10 shows the same ECMWF-derived thermodynamic fields as Figure 8, here at 0600 UTC on 10 October 2008, corresponding to the back-tracing of the gravity wave train observed in the satellite imagery in Figure 9. In this case, the observed gravity wave traces back to a region of negative ΔNBE just upstream of the point where a mid-latitude trough extends north towards the subtropical jet stream.

5.3. *27 October 2008 case*

Figure 11 shows satellite imagery for propagating gravity waves observed in a sequence of selected GOES-10 thermal infrared images between 0545 and 1115 UTC on 27 October 2008 at 3-h intervals, with magnified images within the white boxes of the left panels showing the accompanying right panels of the same figure. Figure 11a shows a series of wave-fronts similarly aligned in a northwest–southeast direction and advancing to the northeast, within the region 71°W to 78°W, 23°S to 29°S. Figures 11(b) and 11(c) show the same waves at later times. In all three panels we see POCs in the troughs of the waves (in the upper left and lower right corners of the right panels of Figure 11(a) and in the upper left only of Figures 11(b) and 11(c)).

Figure 12 again shows the same fields as Figure 8, here at 0600 UTC on 27 October 2008, corresponding to the gravity wave train illustrated in Figure 11 and described above. In this case, the origin of the waves traces back to a point at 30°S, 82°W, where we see a marked anticyclonically breaking (LC1 type) Rossby wave in Figure 12b. A further description of LC1 and LC2 breaking Rossby wave types is presented in Thorncroft *et al.* (1993). Similar to the 8 October case, we see a profile of large negative ΔNBE at this location (Figure 10c) coinciding with the tropopause fold.

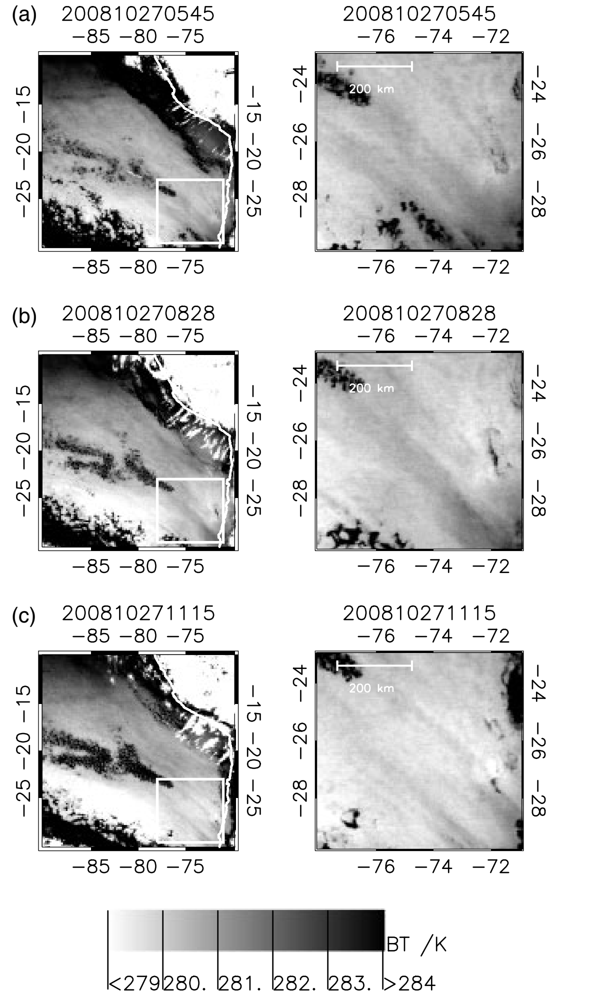

Figure 11. Time sequence at approximately 3 h intervals (see time labels for each panel) of GOES-10 thermal infrared window brightness temperature (greyscaled within the range 276–282 K) across the period 0545 UTC, 27 October 2008 to 1115 UTC, 27 October 2008. The sequence shows a series of gravity waves highlighted within the white box on each left panel, with the corresponding zoomed area in the right panels.

5.4. *Common sources*

In all three cases observed in October 2008, the observed gravity wave trains trace back to a region of large negative residual NBE and hence areas of flow divergence. This points to a gravity wave energy source by geostrophic adjustment. For the 8 October and 27 October cases, these areas of residual NBE are tropopause folds associated with LC2 and LC1 Rossby wave breaking, respectively, along the subtropical jet stream. For the 11 October case, the Rossby wave appears poleward of the subtropical jet stream (STJ) – i.e. in the polar jet stream. Satellite imagery and ECMWF fields were also examined for November 2008, but at times when gravity waves were not observed in GOES-10 imagery, there was neither evidence of nearby Rossby wave activity nor centres of large negative ΔNBE. Indeed there were no further gravity waves observed in the imagery during the VOCALS-REx campaign or throughout November 2008, a period characterized by a quiescent STJ (Toniazzo *et al.*, 2011).

Given the limited period of study examined in this work, it is not possible to place the occurrence of this phenomenon in a climatological context and further studies over a much longer time period would be required to do this. However, climatologies of Rossby wave breaking over the region, seen in this study to be linked to the wave disturbance, do exist. A climatological study dedicated to tropopause folding frequency near the subtropical tropopause by Postel and Hitchman (1999) used a complex fold-tracking detection algorithm applied to ECMWF analyses between 1986 and 1995, which showed a strong seasonal cycle in both hemispheres, with maxima in respective summers. Further work by Peters and Waugh (2003), across a 3 yr time-scale, which focused on the Southern Hemisphere, documents a diverse range of breaking Rossby wave dynamics and structure with a wide seasonal and interannual variability. Given those findings, it is not yet possible to conjecture on the true frequency and variability of this phenomenon in general, especially not at the more localized scale of the southeast Pacific Sc cloud deck. Further studies which examine NBE residuals, as well as Rossby wave breaking over long time-scales, would be required to confirm a common link, which would also need to be cross-referenced to corresponding satellite imagery.

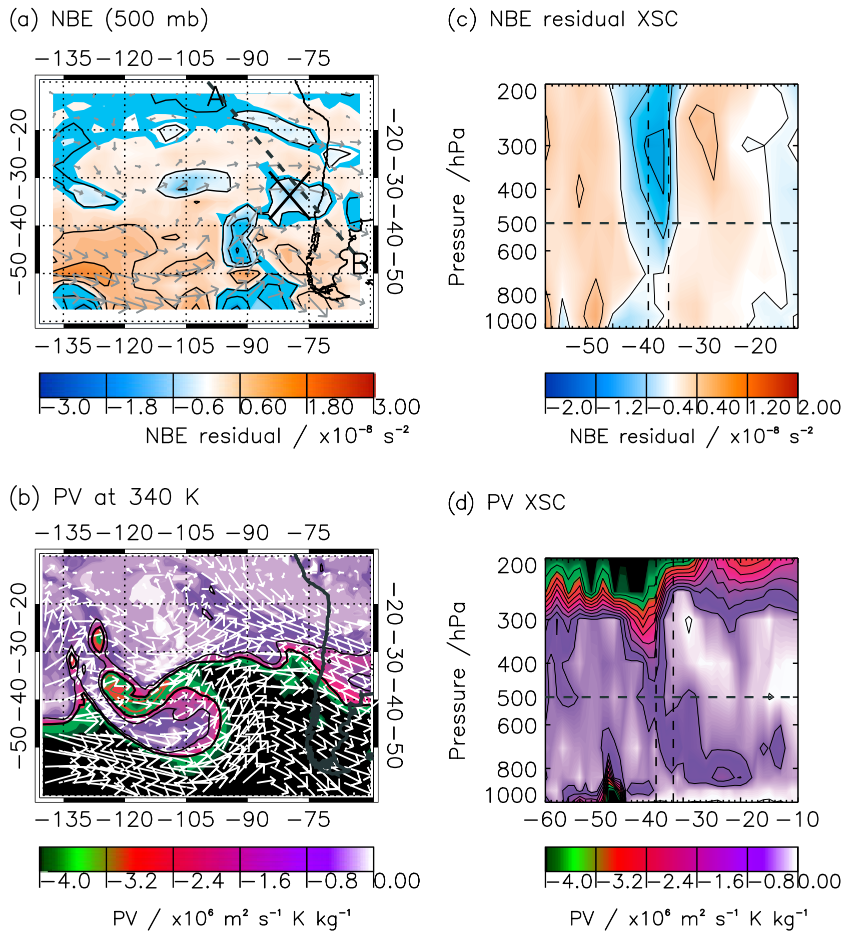

Figure 12. Same as Figure 8 caption for 0600 UTC on 27 October 2008, with the exception that the black cross in (a) marks the mid-point of the backward-traced gravity wave-front observed at 0528 UTC on 27 October 2008. This figure is available in colour online at wileyonlinelibrary.com/journal/qj

6. Conclusions

This study has demonstrated a previously unknown role for atmospheric gravity waves in the southeast Pacific region by their ability to modulate cloud radiative and dynamical properties over a wide area. Using satellite imagery and satellite-retrieved cloud bulk properties during October 2008 over the southeast Pacific, we have illustrated the horizontal propagation of a series of gravity wave trains by their influence on the Sc cloud deck capping the local marine boundary layer. The waves were observed as a non-dispersive periodic modulation of retrieved CTH by up to 500 m peak-to-trough during a case study of waves observed on 8 October 2008, while the horizontal direction of wave propagation was perpendicular to the synoptic boundary layer flow. The waves appeared to originate near 30°S, 85°W and were initiated for a 2-h period beginning at midday on 7 October 2008, propagating along a vector directed approximately northeastward toward the Peruvian Coast (15°S, 70°W) over the following 36 h, covering a distance in excess of 1500 km. During that time, the gravity waves were observed to affect both reversible and non-reversible changes in cloud radiative properties and cloud dynamics such that POCs developed in the troughs of passing gravity wave-fronts. The POCs were observed to form in regions with high background LWP and the gravity waves were observed to enhance this LWP further, consistent with an expected increase in precipitation rate in this low CCN environment. The increase in precipitation rate, by whatever means, is a mechanism common to previous studies of POC development in the southeast Pacific.

Two additional cases (11 and 27 October 2008) of gravity wave propagation were observed in satellite imagery of the southeast Pacific later in October 2008. Lagrangian back-tracking from their point of manifestation on the cloud deck for both these waves and those examined in detail for the 8 October case, show that waves originated in areas displaying large negative residual to the nonlinear balance equation, which were associated with Rossby waves propagating along the subtropical and polar jet streams. We propose here that these gravity waves were generated by geostrophic adjustment around the jet streams. Although this is consistent with mesoscale gravity wave events previously recorded in the literature, the waves in this case propagated equatorward rather than poleward. This case study demonstrates that gravity waves and their impacts on Sc thermodynamics in the southeast Pacific are one formative mechanism for POCs in the region and serves to demonstrate and highlight the important effects that gravity waves propagating in the troposphere can have on cloud radiative properties (and hence surface radiation budgets) over a significant spatial extent. These results also emphasize the importance of synoptic influence on Sc-covered marine boundary layers through changes to the LWP and hence precipitation rate. Further studies are required to place this effect in a climatological context.

Acknowledgement

The UK element of the VOCALS-REx campaign was funded by a Natural Environment Research Council consortium grant (Grant ref: NE/F019874/1). We thank the European Centre for Medium-Range Weather Forecasts (ECMWF) for operational reanalysis data, provided by the British Atmospheric Data Centre (available from http://badc.nerc.ac.uk/data/ecmwf-op/). Yuter and Burleyson were supported by US National Oceanic and Atmospheric Administration grant GC09-252b and US National Aeronautical and Space Administration grants NNX10AP43H and NNX11AE98G. Support for developing the GOES-10 data products was provided by the Department of Energy ARM Program and the NASA Modeling, Analysis, and Prediction Program. Matthew Miller of North Carolina State University is also thanked for assistance in the plotting of Figure 7.

Supporting Information

The following supporting information is available as part of the online article:

Video S1. Animation of GOES-10 Channel 4 satellite imagery over the South East Pacific between 1358 UTC, 7 Oct 2008 and 0015 UTC, 12 Oct 2008 (case 1).

Video S2. Animation of GOES-10 Channel 4 satellite imagery over the South East Pacific between 1128 UTC, 11 Oct 2008 and 1258 UTC, 12 Oct 2008 (case 2).

Video S3. Animation of GOES-10 Channel 4 satellite imagery over the South East Pacific between 1215 UTC, 26 Oct 2008 and 2315 UTC, 27 Oct 2008 (case 3).

References

Allen G, Coe H, Clarke A, Bretherton C, Wood R, Abel SJ, Barrett P, Brown P, George R, Freitag S, McNaughton C, Howell S, Shank L, Kapustin V, Brekhovskikh V, Kleinman L, Lee Y-N, Springston S, Toniazzo T, Krejci R, Fochesatto J, Shaw G, Krecl P, Brooks B, McMeeking G, Bower KN, Williams PI, Crosier J, Crawford I, Connolly P, Allan JD, Covert D, Bandy AR, Russell LM, Trembath J, Bart M, McQuaid JB, Wang J, Chand D. 2011. South East Pacific atmospheric composition and variability sampled along 20°S during VOCALS-REx. *Atmos. Chem. Phys.* **11**: 5237–5262. DOI:10.5194/acp-11-5237-2011.

Bosart LF, Bracken WE, Seimon A. 1998. A study of cyclone mesoscale structure with emphasis on a large-amplitude intertia-gravity wave. *Mon. Wea. Rev.* **126**: 1497–1527.

Bott A. 1998. A flux method for the numerical solution of the stochastic collection equation. *J. Aerosol. Sci*,**55**: 2284–2293.

Bretherton CS, Uttal T, Fairall CW, Yuter SE,Weller RA, Baumgardner D, Comstock K, Wood R. 2004. The EPIC 2001 stratocumulus study. *Bull. Am. Meteorol. Soc,* **85**: 967–977.

Bretherton CS, Wood R, George RC, Leon D, Allen G, Zheng X. 2010. Southeast Pacific stratocumulus clouds, precipitation and boundary layer structure sampled along 20°S during VOCALS-REx. *Atmos. Chem. Phys,* **10**: 10639–10654. DOI:10.5194/acp-10-10639-2010.

Comstock K, Bretherton CS, Yuter SE. 2005. Mesoscale variability and drizzle in Southeast Pacific stratocumulus. *J. Atmos. Sci*, **62**: 3792–3807.

Comstock K, Yuter SE, Wood R, Bretherton CS. 2007. The three dimensional structure and kinematics of drizzling stratocumulus. *Mon. Wea. Rev,* **135**: 3767–3784.

DeSzoeke SP, Yuter SE, Zuidema P, Fairall CW, Brewer WA. 2010. Ship-based observation of drizzling stratocumulus clouds from EPIC to VOCALS. *CLIVAR Exchanges* **15**: 11–13.

George RC, Wood R. 2010. Subseasonal variability of low cloud radiative properties over the southeast Pacific Ocean. *Atmos. Chem. Phys*, **10**: 4047–4063. DOI:10.5194/acp-10-4047-2010.

Haag W, Karcher B. 2004. The impact of aerosols and gravity waves on cirrus clouds at midlatitudes. *J. Geophys. Res*, **109**: D12202. DOI:10.1029/2004JD004579.

Knippertz P, Chagnon JM, Foster A, Lathouwers L, Marsham JH, Methven J, Parker D. 2010. Research flight observations of a prefrontal gravity wave near the southwestern UK. *Weather* **65**: 293–297.

Koch SE, O'Handley C. 1997. Operational forecasting and detection of mesoscale gravity waves. *Weath. Forecast.* **12**: 253–281.

Koch SE, Hamilton D, Kramer D, Langmaid A. 1998. Mesoscale dynamics in the Palm Sunday tornado outbreak. *Mon. Weather Rev,* **126**: 2031–2060.

Lindzen RS, Tung KK. 1976. Banded convective activity and ducted gravity waves. *Mon. Wea. Rev.* **104**: 1602–1617.

Mechem DB, Yuter SE, de Szoeke SP. 2012. Thermodynamic and aerosol controls in southeast Pacific stratocumulus. *J. Atmos. Sci* **69**: 1250–1266.

Meehl GA, Stocker TF, Collins WD, Friedlingstein P, Gaye AT, Gregory JM, Kitoh A, Knutti R, Murphy JM, Noda A, Raper SCB, Watterson IG, Weaver AJ, Zhao Z-C. 2007. Global climate projections. In *Climate Change 2007: The Physical Science Basis. Contribution of Working Group I to the Fourth Assessment Report of the Intergovernmental Panel on Climate Change*, Solomon S, Qin D, Manning M, Chen Z, Marquis M, Averyt KB, Tignor M, Miller H (eds). Cambridge University Press: Cambridge, UK.

Menzel WP, Purdom JFY. 1994. Introducing GOES I: The first of a new generation of Geostationary Operational Environmental Satellites. *Bull. Am. Meteorol. Soc*, **75**: 757–781.

Miles NL, Verlinde J, Clothiaux EE. 2000. Cloud droplet size distributions in low-level stratiform clouds. *J. Atmos. Sci*, **57**: 295–311.

Minnis P, Szedung S-M, Young DF, Heck PW, Garber DP, Yan Chen; Spangenberg DA, Arduini RF, Trepte QZ, Smith WL, Ayers JK, Gibson SC, Miller WF, Hong G, Chakrapani V, Takano Y, Kuo-Nan L, Yu X, Yang P. 2011. CERES Edition-2 cloud property retrievals using TRMM VIRS and Terra and Aqua MODIS data, Part I: Algorithms. *IEEE Trans. Geosci. Remote Sens,* **49**(11): DOI: 10.1109/TGRS.2011.2144601.

Moore JT, Abeling WA. 1988. A diagnostic of unbalanced flow in upper levels during the AVE-SESAME I period. *Mon. Weath. Rev*, **116**: 2425–2436.

Peters D, Waugh DW. 2003. Rossby wave breaking in the Southern Hemisphere wintertime upper troposphere. *Mon. Wea. Rev,* **131**: 2623–2634.

Petters MD, Snider JR, Stevens B, Vali G, Faloona I, Russell L. 2006. Accumulation mode aerosol, pockets of open cells, and particle nucleation in the remote subtropical Pacific marine boundary layer. *J. Geophys. Res*, **111**: D02206.

Postel GA, Hitchman MH. 1999. A climatology of Rossby wave breaking along the subtropical tropopause. *J. Atmos. Sci,* **56**: 359–373.

Rahn DA, Garreaud RD, Rutllant JA. 2011. The low-level atmospheric circulation near Tongoy Bay–Point Lengua de Vaca (Chilean Coast, 30°S). *Mon. Wea. Rev,* **139**: 3628–3647.

Randall DA, Wood RA, Bony S, Colman R, Fichefet T, Fyfe J, Kattsov V, Pitman A, Shukla J, Srinivasan J, Stouffer RJ, Sumi A, Taylor KE. 2007. Climate models and their evaluation. In *Climate Change 2007: The Physical Science Basis. Contribution of Working Group I to the Fourth Assessment Report of the Intergovernmental Panel on Climate Change*, Solomon SS, Qin DD, Manning MM, Chen ZZ, Marquis MM, Averyt KKB, Tignor MM, Miller HH (eds). Cambridge University Press: Cambridge, UK.

Stevens B, Vali G, Comstock K, Wood R, Van Zanten M, Austin PH, Bretherton CS, Lenschow DH. 2005. Pockets of open cells (POCs) and drizzle in marine stratocumulus. *Bull. Am. Meteorol. Soc*, **86**: 51–57.

Thorncroft CD, Hoskins BJ, McIntyre ME. 1993. Two paradigms of baroclinic-wave life-cycle behaviour. *Q. J. R. Meteor. Soc.* **119**: 17–55.

Toniazzo T, Abel SJ, Wood RA, Mechoso SR, Allen G, Shaffrey LC. 2011. Large-scale and synoptic meteorology in the south-east Pacific during the observations campaign VOCALS-REx in Spring 2008. *Atmos. Chem. Phys*, **11**: 4977–5009.

Uccellini LW, Koch SE. 1987. The synoptic setting and possible energy sources for mesoscale wave disturbances. *Mon. Wea. Rev,* **115**: 721–729.

Wang H, Feingold G, Wood R, Kazil J. 2010. Modelling microphysical and meteorological controls on precipitation and cloud cellular structures in Southeast Pacific stratocumulus. *Atmos. Chem. Phys*, **10**: 6347–6362.

Wood R. 2012. Stratocumulus clouds. *Mon. Wea. Rev.* in press.

Wood R, Comstock KK, Bretherton CS, Cornish C, Tomlinson J, Collins DR, Fairall C. 2008. Open cellular structure in marine stratocumulus sheets. *J. Geophys. Res*, **113**: D12207.

Wood R, Bretherton CS, Leon D, Clarke AD, Zuidema P, Allen G, Coe H. 2011a. An aircraft case study of the spatial transition from closed to open mesoscale cellular convection. *Atmos. Chem. Phys*, **11**: 2341–2370.

Wood R, Mechoso CR, Weller RA, Huebert B, Straneo F, Albrecht BA, Coe H, Allen G, Vaughan G, Fairall C, Chand D, Gallardo Klenner L, Garreaud R, Gradcos C, Covert DS, Bates TS, Krejci R, Russell LM, de Szoeke S, Brewer A, Yuter SE, Springston SR, Chaigneau A, Toniazzo T, Minnis P, Palokonda R, Abel SJ, Brown WO, Williams SF, Fochesatto J, Brioude J, Bower KN. 2011b. The VAMOS Ocean–Cloud–Atmosphere–Land Study Regional Experiment (VOCALSREx): goals, platforms, and field operations. *Atmos. Chem. Phys,* **11**: 627–654.

Zack JW, Kaplan ML. 1987. Numerical simulations of the subsynoptic features associated with the AVE-SESAME I case. Part I: The pre-convective environment. *Mon. Weath. Rev.* **115**: 2367–2394.

Zdunokowski W, Bott A. 2003. *Dynamics of the Atmosphere: A Course in Theoretical Meteorology*. Cambridge University Press: Cambridge, UK.

Zhang F, Koch SE, Davis CA, Kaplan ML. 2001. Wavelet analysis and the governing dynamics of a large-amplitude mesoscale gravity-wave event along the East Coast of the United States. *Q. J. R. Meteorol. Soc.* **127**: 2209–2245.

Zhang F, Koch SE, Kaplan ML. 2003. Numerical simulations of a large-amplitude mesoscale gravity wave event. *Meteorol. Atmos. Phys*, **84**: 199–216.

Zuidema P, Westwater ER, Fairall C, Hazen D. 2005. Ship-based liquid water path estimates in marine stratocumulus. *J. Geophys. Res*, **110**: D20206. DOI:10.1029/2005JD005833.

